Multipeak Raindrop Size Distribution Observed by UHF/VHF Wind Profilers during the Passage of a Mesoscale Convective System

B. RADHAKRISHNA AND T. NARAYANA RAO

National Atmospheric Research Laboratory, Gadanki, India

ABSTRACT

The Indian Mesosphere–Stratosphere–Troposphere radar (IMSTR), Lower Atmospheric Wind Profiler (LAWP), and Joss–Waldvogel (JW) disdrometer measurements during the passage of two distinctly different (in terms of total rain and rainfall rate) convective storms are utilized to understand the nature and origin of the multipeak raindrop size distribution (MRDSD). Important issues, such as the preferential stage and height at which bi- or multimodal rain distribution occurs in a mesoscale convective system (MCS) are addressed. For both of the storms, the MRDSD is observed during the transition period from convection to stratiform rain. The pattern and variation of the MRDSD during this period is strikingly similar in both of the storms. The MRDSD is first observed above the freezing level in the presence of heavy riming. The subsequent spectra have shown bimodal distribution below the freezing level, and the bimodality is attributed to the coexistence of ice and supercooled droplets. Interestingly, the bimodal distribution has not varied much with altitude when it is produced because of the coexistence of ice and supercooled droplets. The MRDSD is also observed at few range gates and for a short duration. Such a type of MRDSD is seen during the transition period between decaying and intensifying rain.

1. Introduction

The raindrop size distribution (DSD) is often represented with a simple functional form [e.g., exponential (Marshall and Palmer 1948), lognormal (Feingold and Levin 1986), and gamma (Ulbrich 1983)]. In reality, the shape of the distribution, on occasions, is much more complex and deviates considerably from the simple functional form used in earlier investigations. These complex distributions generally show two (bimodal) or three (trimodal) peaks in the distribution [or in general, multipeak raindrop size distribution (MRDSD)].

The MRDSD at the surface has been studied for several years using disdrometers, such as the one described by Joss and Waldvogel (JW) (1969) (Steiner and Waldvogel 1987; Sauvageot and Koffi 2000 and references therein). The DSD measured with the JW disdrometer can be multimodal for various reasons. They form as a result of atmospheric processes (e.g., microphysical processes, dynamics, and kinematics) and also

from the biases in measurement techniques (e.g., instrumental and sampling problems). For example, measurements taken over a shorter interval or in a smaller sampling area often produce multimodal DSD. Also, it is now well known that the JW disdrometer suffers from a small, but permanent, bias in DSD due to the transfer function of electronic circuits (Sheppard 1990). The transfer function that converts an electronic signal into a drop size exhibits slight undulations that, if not properly considered, result in some of raindrops being counted in the wrong size bin, which may yield a multipeaked structure of raindrop spectra. This bias may results into MRDSD, particularly for averaged DSDs. The dynamical effects that can produce the MRDSD are associated with the overlapping of rain shafts from contiguous rain cells, present either at the same vertical level with wind shear below that level or overlying one another (Marshall 1953; Atlas and Plank 1953; Gunn and Marshall 1955; Douglas et al. 1957; McFarquhar et al. 1996). However, these studies have not accounted the changes in DSD due to microphysical processes (e.g., collision–coalescence, breakup, and secondary ice generation) in the falling precipitation.

On the contrary, modeling studies employing Low and List's (1982b) analytical expressions, which in turn

Corresponding author address: Dr. T. Narayana Rao, National Atmospheric Research Laboratory, S.V.U. Campus, P.O. Box No. 123, Prakasham Nagar, Tirupati 517 502, A.P., India.
E-mail: tnrao@narl.gov.in

are based on a series of laboratory experiments conducted by Low and List (1982a), have demonstrated that the MRDSD is a result of drops produced from fragmentation of filaments, sheets, and disks (Donaldson 1984; Valdez and Young 1985; List et al. 1987; Brown 1988; also see the review by Testik and Barros 2007). In spite of using different numerical solutions and different resolutions in their models, these studies converged to produce a trimodal distribution, although the relative magnitude and location of peaks in the distribution are not precisely the same. Several studies with JW disdrometers also observed peaks similar to those observed in modeling studies (Steiner and Waldvogel 1987; Zawadzki and Antonio 1988; Sauvageot and Koffi 2000), supporting the above processes. McFarquhar and List (1993), however, have shown that the magnitudes of peaks associated with instrumental errors and the observed peaks are of the same order, raising doubts about the role of microphysical processes producing peaks in the distribution. Later, raindrop measurements with optical probes also show MRDSD similar to those predicted by the models (Willis 1984; Garcia-Garcia and Gonzalez 2000). A recent study employing a new numerical parameterization scheme, which alleviates the shortcomings of Low and List's (1982b) parameterization scheme, has shown a bimodal distribution with peaks at 0.26 and 2.3 mm (McFarquhar 2004). This study showed that filament breakup and coalescence of raindrops are responsible for the peaks. Recently, Prat and Barros (2007) presented a discrete numerical model for collision–breakup and tested their model with the popular coalescence and breakup parameterization schemes available in the literature (Low and List 1982b; McFarquhar 2004). Their analysis shows a bimodal equilibrium distribution with peaks at 0.26 and 2.5 mm, consistent with the results of McFarquhar (2004).

The Doppler radars operating at UHF and higher frequencies are highly sensitive to precipitation and obtain strong backscatter from hydrometeors. These radars are highly useful in studying the height and temporal evolution of precipitation structure and microphysical variations. Such information is crucial to understand the MRDSD in a better way. The bimodality of the precipitation spectrum has been studied with wind profilers (Gossard et al. 1990) and X-band radars (Zawadzki et al. 2001). Gossard et al. (1990) have shown that melting/breakup processes at the freezing level and coalescent growth of cloud droplets are the main mechanisms for the observed bimodality in the precipitation echo. Zawadzki et al. (2001) observed multiple peaks in the precipitation echo at all altitudes below 6 km and ascribed them to microphysical processes occurring above the melting level. They attributed the bimodality to the

secondary ice generation and to the supercooled drizzle. However, information on vertical air velocities, a crucial parameter for obtaining DSD and also inferring several microphysical processes, are estimated indirectly in the above studies (Zawadzki et al. 2000, 2001). Direct measurement of vertical air motion is possible with VHF wind profilers in all weather conditions. Probing a common volume with VHF and UHF (or higher frequency) profilers, therefore, has several advantages over single radar profiling. Such an approach will provide information on both the microphysics and dynamics of precipitation and also their variation with height and time.

The present research aims to study the nature and origin of MRDSD, which has been observed aloft in the radar spectra as well at the surface in the disdrometer data. In particular, the focus of the paper is on the stage and height of the mesoscale convective system (MCS) at which the MRDSD has been observed and the subsequent evolution of the MRDSD with height and time. The evolution of MRDSD has been studied with the help of rain DSD obtained from UHF and VHF wind profiler measurements, by employing the dual-frequency technique (Rajopadhyaya et al. 1993; Schafer et al. 2002). Such information is not available in the tropics. To the author's knowledge, the present article is the first observational report on MRDSD using UHF and VHF wind profilers. The details on the data and instruments used for the present study are given in section 2. A rain event containing both convection and stratiform precipitation, during which both radar and disdrometer maps show MRDSD, is discussed in detail in section 3. The ramifications of this study are discussed briefly in section 4 along with the summary of present observations.

2. Data and analysis

The measurements used for the present study are obtained with a UHF wind profiler [i.e., Lower Atmospheric Wind Profiler (LAWP)], high power VHF radar [i.e., Indian MST Radar (IMSTR)], and an impact-type disdrometer (RD69; Joss and Waldvogel 1967, 1969), all are collocated at Gadanki, India (13.5°N, 79.2°E). The complete description of the systems used for the present study can be found elsewhere (i.e., IMSTR in Rao et al. 1995; LAWP and disdrometer in Rao et al. 2001). The JW disdrometer provides rain DSD in 20-diameter intervals ranging from 0.3 to 5 mm at every 1-min interval. It converts the impact of raindrop hitting the styrofoam body of an area 50 cm^2 to an electric pulse, whose amplitude is proportional to the drop size. The data processing and parameter (i.e., DSD, rain rate, reflectivity factor, etc.) extraction procedures are given in Rao et al. (2001), which of course are based on

standard procedures prescribed in the literature and disdrometer manual. The dead-time correction was not applied to the present dataset, as it does not change the DSD in channels, in which the drop count is zero (Tokay and Short 1996).

The important parameters of the radars and the specifications used for the present study are summarized in Table 1. Note that the LAWP operates continuously switching between low and high modes. The IMSTR is operated in a multibeam mode with 12 beams, in which 8 beams are pointed along the zenith direction (i.e., Z_x: north–south polarization and Z_y: east–west polarization). The pattern of beam switching is as follows: Z_x, Z_y, Z_x, Z_y, Z_x, Z_y, east, west, Z_x, Z_y, north, and south. The backscattering mechanism is the same for both the radars in fair-weather conditions; however, the LAWP is more sensitive to precipitation (through Rayleigh scattering) than the IMSTR. The IMSTR obtains strong backscatter from precipitation during moderate to heavy rain (Rao et al. 1999). Ralph (1995) also show that the precipitation echo power dominates the turbulence echo power in strong rain (i.e., when the rainfall rate exceeds 8.4 mm h^{-1}). In such a scenario, the traditional single peak picking algorithms, generally used to retrieve moments from wind profiler spectra, may either treat both these echoes as a single echo or pick the wrong echo. In both the cases, the error will be significant. In the present study, the echoes are separated following Rao et al. (1999).

The rain DSD has been retrieved whenever simultaneous measurements of IMSTR and LAWP were available using the dual-frequency technique (Rao et al. 2006; Kirankumar et al. 2008, and references therein). The retrieval technique and the error analysis are described in detail in above studies, and therefore, only a brief description is provided here. The measured Doppler spectrum of any profiler can be mathematically represented as (Wakasugi et al. 1986)

$$S(w) = [G(w - \overline{w}) + G_0(w) * P(v - \overline{w})] * F, \quad (1)$$

where $G(w - \overline{w})$ is the clear-air Doppler spectrum; $G_0(w)$ is the normalized clear-air spectrum; $P(v)$ is the reflectivity weighted fall speed spectrum; v and $\overline{w}$ are particle fall speed and mean vertical air motion, respectively; F is the data window function; and the asterisk denotes the convolution operator. The first term in Eq. (1) is negligible in case of LAWP, because the precipitation echo generally masks the clear-air portion of the spectrum. To obtain the spectra due to precipitation, the second term (representing the convolution of the normalized clear-air spectrum and precipitation spectrum) needs to be corrected for vertical air motion, turbulence,

TABLE 1. Important specifications and parameters of IMSTR and LAWP on 21–22 Jun 2000.

Parameter	MST radar	LAWP
Frequency	53 MHz	1357.5 MHz
Peak power	2.5 MW	1 kW
Beamwidth	3°	4°
Interpulse period	250 μs	60 (80)* μs
Pulse width	2 μs	1 (2)* μs
No. coherent integrations	512	70 (50)*
No. incoherent integrations	1	100 (64)*
No. FFT points	256	128
No. of beams	12 (Z_x, Z_y, Z_x, Z_y, Z_x, Z_y, E10, W10, Z_x, Z_y, N10, and S10)	3 (Z_x, N15, and E15)
Range resolution	300 m	150 m (sampling at 1 μs)
Velocity resolution	0.086 m s^{-1}	0.205 (0.215)* m s^{-1}

* Specifications of LAWP for the high mode.

and nonturbulence contributions (i.e., beam broadening effects). To extract vertical air motion and spectral width due to turbulence and other effects, the IMSTR spectrum is fitted with the Gaussian distribution:

$$G(w) = A_0 \exp(-w^2/2\sigma_\omega^2), \quad (2)$$

where A_0 and σ_ω are the amplitude and spectral width of the Bragg's scatter. To remove the broadening contribution due to turbulence and other nonturbulent processes from the LAWP spectrum and also to correct for vertical air motion, the LAWP spectrum is deconvolved with the IMSTR spectrum. The Fourier transform (FT) technique is used to deconvolute the LAWP spectrum (Schafer et al. 2002):

$$S^p(w) = \text{SHIFT}_{(-\overline{w})} \left\langle \text{FFT}^{-1} \left\{ \frac{\text{FFT}[P_{pc}(v - \overline{w})]\Phi(w)}{\text{FFT}(G_0(w))} \right\} \right\rangle, \quad (3)$$

where $P_{pc} = G_0(w) * P(v - \overline{w})$, FFT denotes the fast Fourier transform, FFT^{-1} represents inverse FFT, SHIFT represents the mean shift of the Doppler spectra based on the vertical air velocity [obtained from Eq. (2)], and $\Phi(w)$ is the optimal filter. The spectrum thus obtained represents the reflectivity-weighted fall speed spectrum due to hydrometeors. It can be, theoretically, represented in terms of the drop diameter with the following equation:

$$S^p(D) = \frac{1}{Z_e} N(D) D^6 \frac{dD}{dv}, \quad (4)$$

where D is the diameter of the drop, v is the terminal velocity, and Z_e is the radar reflectivity factor estimated from LAWP measurements. Surface disdrometer measurements were used for absolute calibration of LAWP backscattered power (i.e., for obtaining radar reflectivity factor, Z_e), following Gage et al. (2000). The value of dD/dv is estimated using the empirical relation between the terminal fall speed and drop size (Atlas et al. 1973; Foote and du Toit 1969):

$$v = (9.65 - 10.3e^{-0.6D})\left(\frac{\rho}{\rho_0}\right)^{-0.45}, \qquad (5)$$

where ρ and ρ_o are the atmospheric densities at the height of observation and near the ground, respectively. The constants used in the equation are valid only when v is in meters per second and D is in millimeters. After knowing the reflectivity at each spectral point, the estimation of $N(D)$ is straightforward using the Eq. (4). Note that, the spectrum is not assumed to follow any functional form (i.e., exponential, gamma, etc.) in the present study. As the present study discusses the multipeak behavior of rain DSD, the direct deconvolution technique (Rajopadhyaya et al. 1993) is employed for retrieving rain DSD.

As the present article aims to study the nature of MRDSD during different types of precipitating systems, the classification of precipitating systems is essential. In the present study, the classification scheme discussed in Rao et al. (2008), which is a modified version of Williams et al. (1995), is employed. The classification algorithm first separates the warm and cold rains based on whether the rain top (defined by 20 dBZ) is below or above the climatological 0°C isotherm level. The cold rain is further divided into deep convection, deep stratiform, and transition types. The deep convection is characterized by large reflectivities (>38 dBZ) or intense Doppler velocities (≤ -10 m s^{-1} or ≥ 1 m s^{-1}). The presence of the radar bright band indicates the rain is associated with the stratiform rain. The rain is classified as transition if profiles of spectral moments show both brightband and convection signatures (i.e., transition inclusive) and also neither brightband nor convective signatures (i.e., transition exclusive; see Rao et al. 2008 for more details on the algorithm).

The peaks in DSD (retrieved from the disdrometer) are identified following the procedure discussed in Steiner and Waldvogel (1987). The peak at $N(D_i)$ should satisfy the condition $N(D_{i-1}) < N(D_i) > N(D_{i+1})$, where i corresponds to the channel number. Since reliable DSD can be retrieved only in the rain region (below 3.9 km) with the radar measurements, a different approach is followed to define the peak in the radar spectrum. The

peaks are identified following the procedure outlined in Lucas et al. (2004). First, gradients of power spectral density (after smoothing the spectrum) with respect to velocity are calculated. The spectral bin corresponding to the zero crossing of estimated gradients from the negative to positive side represents the peak in the spectra.

3. Results and discussion

The rain event during 21–23 June 2000, wherein the MRDSD is observed, is a mesoscale convective system, consisting both convection and stratiform precipitation. During this period, the rain was observed for about 14 h accumulating a rainfall of ~43 mm. The rain occurred primarily in two contrasting spells. The rain duration in the first spell, observed on 21–22 June 2000, is ~6 h (1950–0200 LT), generating a rainfall of ~2.8 mm with a maximum rainfall rate (R) of ~7 mm h^{-1}. The second spell observed on 22–23 June 2000, an intense one in terms of rainfall, lasted for ~8 h (2140–0600 LT) producing ~40 mm of rainfall with a maximum R of 70 mm h^{-1}. Different aspects of this interesting rain event have been studied and documented by several investigators. The synoptic evolution of this event is discussed in Fig. 3 of Dhaka et al. (2003). The variation of rain DSD with altitude and time is discussed in Fig. 5 of Kirankumar et al. (2008) and also in a statistical study on DSD by Rao et al. (2006). The IMSTR, LAWP, and the disdrometer were operated continuously for a major part of the event.

The temporal variation of rain DSD [$N(D)$ in log scale] and rainfall integral parameters [reflectivity factor (Z), mass weighted mean diameter (D_m), and R] is shown in Fig. 1. The data between 0200 and 2130 LT 22 June 2000 are not shown in the figure as there is no rain observed during that period. Furthermore, the data are plotted only until 0000 LT 23 June 2000, because the MRDSD is observed mostly prior to that time. Although both rain spells are associated with the convection (discussed in detail later in this section), the rainfall is more intense in the second spell. However, the magnitudes of D_m and to some extent Z in the first spell are larger with values nearly equal to that of in the second spell, primarily due to the presence (and/or relatively fewer number) of bigger (smaller) raindrops. While in the second convective spell, larger values of R, Z, and D_m are observed, just like in any other convective system.

The rainfall parameters show quasi-periodic oscillations indicating the inhomogeneity in the rainfall. The other possibility is that the rain might have originated in isolated rain shafts, which are organized either on their own or by gravity waves generated by the primary
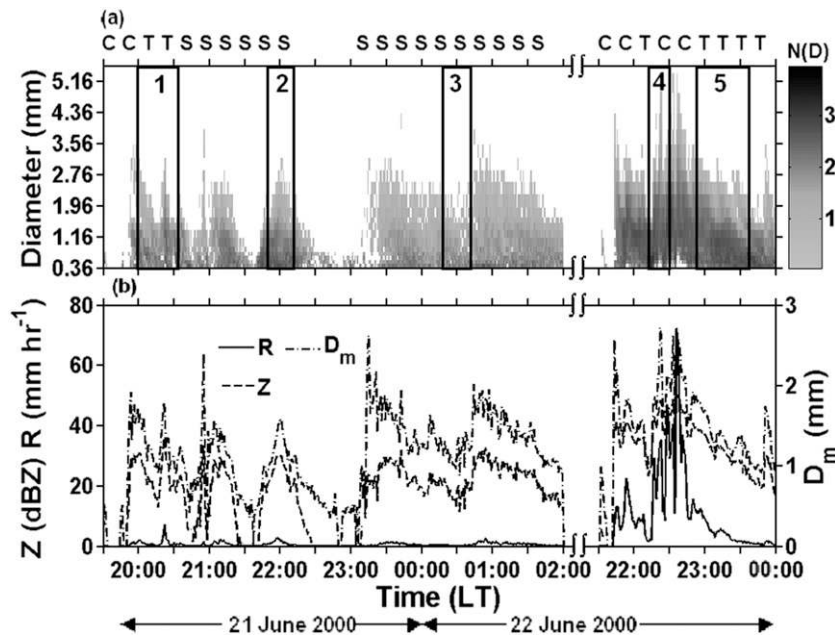
FIG. 1. (a) The temporal variation of rain DSD observed during the passage of two convective storms on 21–22 Jun 2000. Note that $N(D)$ is shown in logarithmic units. The boxes numbered 1–5 correspond to the periods when the MRDSD is observed either in radar spectra and/or in disdrometer measurements. The letters "C," "T," and "S" denote convection, transition, and stratiform precipitation, respectively. (b) Corresponding surface rain rate (R), reflectivity factor (Z), and the mass-weighted mean diameter (D_m) estimated with disdrometer measurements.

convective cell. The instrumentation used in the present study (including vertically pointing radars) does not provide the information of whether the rain is originated from a single cloud with large inhomogeneity or multiple cells. In the absence of such information, we consider that the increasing (decreasing) trend of rainfall is associated with an intensifying (decaying) cell/streamer. The power spectral analysis on rainfall data on 21–23 June 2000 show two prominent peaks at 10- and 40–50-min periodicities (Dhaka et al. 2003). They also observed maximum variance in the vertical wind at 10-min periodicity in the upper troposphere and attributed the wave mode to gravity waves triggered by the convection. The identical power spectral plots of w and R (not shown here, but can be found in Figs. 9 and 10 of Dhaka et al. 2003) indicates that both parameters are modulated by convectively generated gravity waves (CGWs).

The boxes (1–5) in Fig. 1a indicate the periods when the MRDSD is observed either in disdrometer data or in radar spectra. The surface rain DSD spectra at different time intervals are shown in Fig. 2. The MRDSD is seen only in the radar spectra during 2148–2214 LT (box 2), and therefore corresponding surface DSD is not included in Fig. 2. Note that, both individual (solid lines)

and average (thick dashed line) DSD are shown in the figure. It is evident from the figure that the averaging period is not constant, but changes from 2 to 5 min. The period is chosen in such a way that within the period the individual 1-min rain DSDs are nearly similar.

The rain DSD during the period corresponding to box 1 (simply in box 1; Fig. 2a) clearly shows two–three peaks in the distribution. The primary peak at 0.5-mm diameter remained unaltered lying mostly in the diameter range 0.5–0.8 mm during the observation period, albeit with varying number density. However, the other peak at ~2 mm (during 1958–2001 LT) migrated to smaller drop end with time. Similar observation can be seen during 2019–2034 LT, when the rain DSD shows three peaks where the peak at the bigger drop end migrates progressively to smaller drop end. The rainfall in box 3 representing the stratiform rain (Fig. 2b) also depicts two peaks in rain DSD plots. The bigger-sized drops (>2 mm) are almost absent during this period. The secondary peak at ~1 mm diameter, which is prominent during the period 0033–0044 LT, has not migrated to the smaller drop end, in contrast to the peak migration in DSD during the period 1958–2034 LT (box 1).

The rain DSD corresponding to boxes 4 and 5 represents the variation of DSD in the intensifying (Fig. 2c)
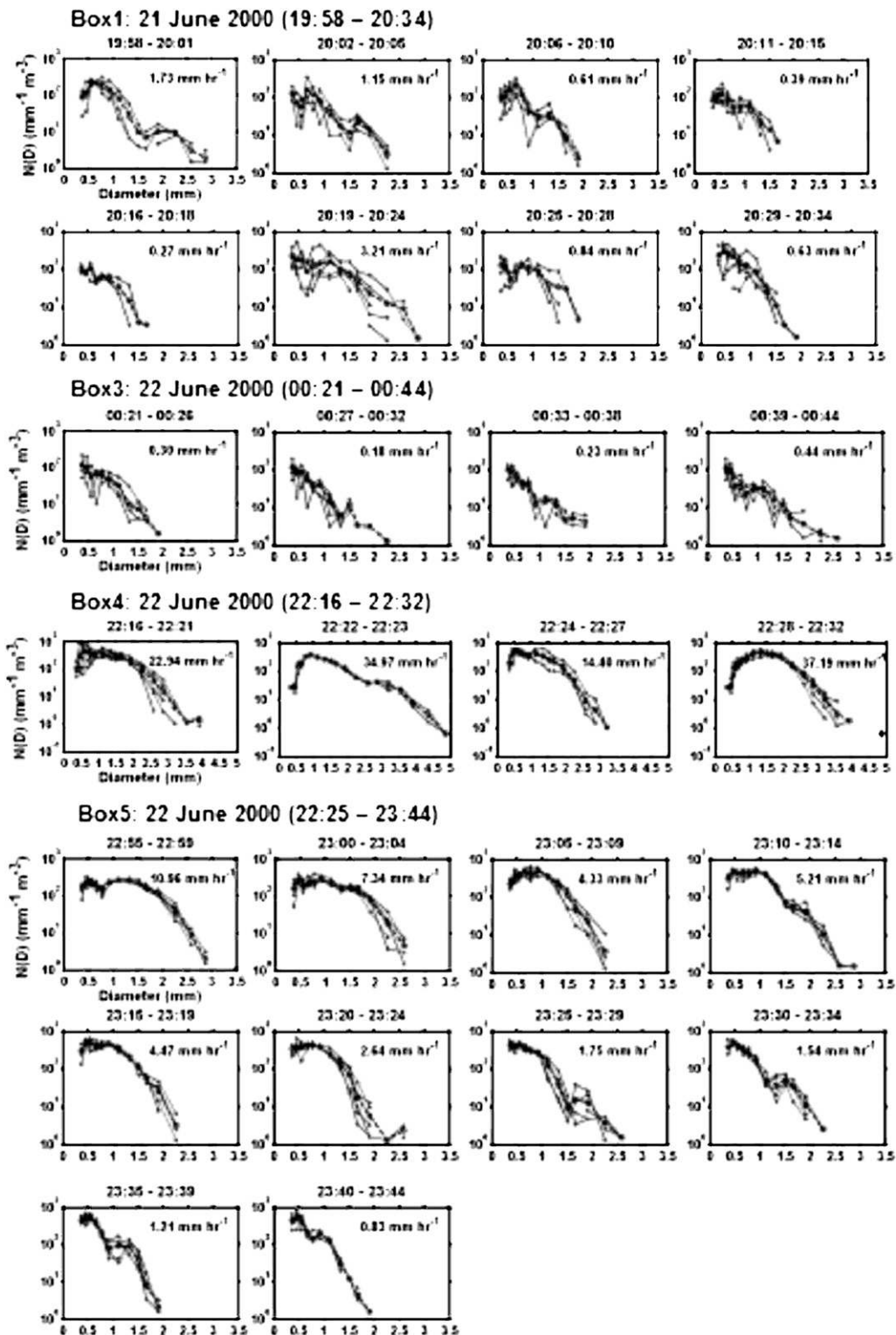
FIG. 2. The temporal variation of rain DSD at the surface corresponding to boxes (a) 1, (b) 3, (c) 4, and (d) 5. Each box contains two–five individual DSD spectra along with their average (dashed line) DSD and the average rain rate. The MRDSD is observed only above the freezing level during the period corresponding to box 2, and therefore the surface DSDs during that period are not included in the figure.
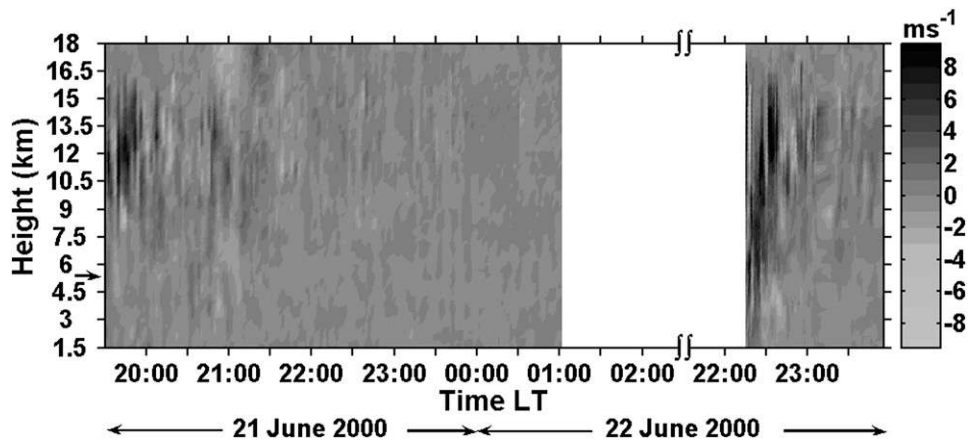
Fig. 3. Time–height cross section of vertical air velocity during the passage of two convective storms observed on 21–22 Jun 2000. The measurements of the zenith-pointing beam of IMSTR are used for constructing the contour map. The white area indicates the data gap. The arrow indicates the climatological 0°C isotherm level.

and decaying (Fig. 2d) stages of a deep convective system. In the intensifying stage (box 4), although the observed MRDSD is similar for a few minutes, there is no sign of migration of peaks with time. Note that the background rain is also highly variable during this period. In the decaying part of the system, the DSD shows a secondary peak, which remained unmoved at ~1.8 mm for most of the observation (until 2329 LT), albeit with decreasing number density. But after 2329 LT, the peak migrated progressively to the lower drop end with time. Apart from the differences in multipeak behavior in the distribution, the DSD itself show interesting differences. A relatively large number of bigger drops are present in the initial stage of convection compared to that in decaying stage. Drop sorting and the increase of collision–coalescence processes in the presence of strong updrafts in the initial phase of convection increases the size of the drops considerably (McFarquhar and List 1991; Kollias et al. 2001). Furthermore, in the initial phase of convection, $N(D)$ increases initially with increase in diameter and then decreases. However, in the decaying stage, the $N(D)$ either remained constant or increased not so significantly with change in diameter at the lower drop end. Accordingly, the D_m values are found to be large in the growth phase [with a mean value of 1.98 mm and standard deviation (σ) of 0.32 mm] and relatively small (1.31 ± 0.22 mm) in the decaying stage.

To better understand the nature of MRDSD and its evolution (as function of altitude), simultaneous profiler data have been considered for further investigation. Also, it is much easier to delineate the rain event into different rain categories (e.g., convection and strati-

form) with the wind profiler data (Williams et al. 1995; Rao et al. 2008). Figure 3 shows the time–height variation of vertical air velocity obtained with a zenith beam of IMSTR during the observational period. It is clearly evident from the figure that the vertical air velocities as large as 8–10 m s^{-1} are observed on both the days (21 and 22 June 2000) in the upper troposphere, indicating the presence of deep convection. The distribution of upper-tropospheric vertical air velocities are also similar during convection (not shown), with ~70% of the population of vertical air velocities within 1–9 m s^{-1} on both days. Although intense updrafts are prevalent on 21 June 2000, as also noted earlier, the associated rainfall was not heavy. Nevertheless, it is very clear from the vertical wind data that on both days intense convection was prevalent.

It is intriguing to note undulations in the vertical wind (Fig. 3) during and also after the passage of convective cells. They are associated with gravity waves triggered by the convection (Dhaka et al. 2003). It can be noticed from the figure that the amplitude of these oscillations is large near the cells and reduces continuously as they propagate away from the source. For example, during 21–22 June 2000, the vertical wind varies from −4 to 4 m s^{-1} during 1950–2020 LT in the upper troposphere, while it is within ±1 m s^{-1} during 2330–0100 LT.

To study the vertical structure of precipitation during the observational period, LAWP measurements are considered. Although IMSTR gets backscatter from precipitation (through Rayleigh scattering) during moderate to high rain, it is not sensitive enough to obtain backscatter from drizzle (Rao et al. 1999). Figure 4 shows the time–height variation of reflectivity factor, Z_e, (dBZ$_e$) and
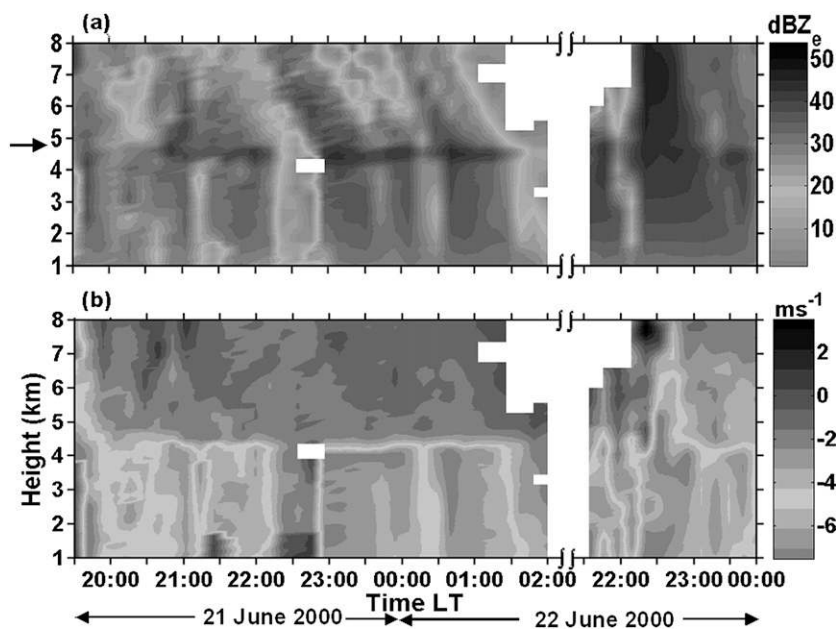
FIG. 4. Time–height cross section of (a) radar reflectivity factor and (b) Doppler velocity of hydrometeors obtained with the LAWP on 21–22 Jun 2000. The gradual reduction of reflectivity factor with decreasing altitude [in (a)] is associated with the receiver saturation problem. The arrow in (a) indicates the climatological 0°C isotherm level.

Doppler velocity (m s^{-1}) of hydrometeors. The reflectivity map clearly shows different types of precipitation (i.e., convection, stratiform, and transition rain; Williams et al. 1995; Rao et al. 2008). The stratiform rain is characterized by the presence of the radar bright band in the vicinity of 0°C isotherm level (4.85 km at Chennai, India, 120 km away from the radar site; see Fig. 4 of Rao et al. 2008). The bright band can be seen clearly during 2045–2215 and 2300–0130 LT 21–22 June 2000, where reflectivity is enhanced by >5 dB near the 0°C isotherm level relative to the reflectivities above and below that level. The other indicator for stratiform precipitation is a sharp gradient in Doppler velocity just below the 0°C isotherm level, as is evident from the figure. The convective rain is generally characterized by large Z_e values and Doppler velocities due to the presence of bigger precipitation particles formed primarily by riming process. The thresholds for Z_e and Doppler velocities for identifying convection are discussed in detail in Rao et al. (2008). Following the precipitation classification scheme of Rao et al. (2008), the convection periods are identified as 1930–1950 LT 21 June 2000 and 2130–2245 LT 22 June 2000, except for a small period of 10 min around 2205 LT 22 June 2000. The periods immediately following convection and prior to the stratiform rain are considered to be associated with transition rain (i.e., 1950–2045 LT 21 June 2000 and 2245–0000 LT 22–23 June 2000).

The individual Doppler power spectra corresponding to boxes 1–5 are now investigated for better understanding of the origin of observed MRDSD. Figures 5–9 depict the variation of Doppler power spectra obtained with the LAWP (top panels) and IMSTR (bottom panels), within the periods corresponding to boxes 1–5, respectively. In each plot, the shading indicates the backscattered power. The 2D spectrum is also overlaid on the plot at each altitude. The 2D power spectrum at each altitude is normalized to its own maximum power value. Note that the LAWP measures the Doppler velocity of hydrometeors (resultant of ambient vertical air motion and the fall velocity of hydrometeors) during rain, rather than the fall velocity of hydrometeors. However, the fall velocity can be obtained by correcting the Doppler velocity for vertical air motion. The solid, dashed, and dash–dot lines on the LAWP spectra represent the traces of primary, secondary, and tertiary peaks in the precipitation echo, respectively. The echo near the zero Doppler velocity in the height region 1.5–3 km in some of the LAWP spectra corresponds to the clear-air echo (i.e., the echo due to irregularities in the refractive index). The solid line on the IMSTR spectra represents the trace of clear air echo (in other words, the ambient vertical air motion).

Most of the Doppler spectra plots corresponding to box 1, the time when high-amplitude gravity waves prevailed in the middle and upper troposphere (Fig. 3),
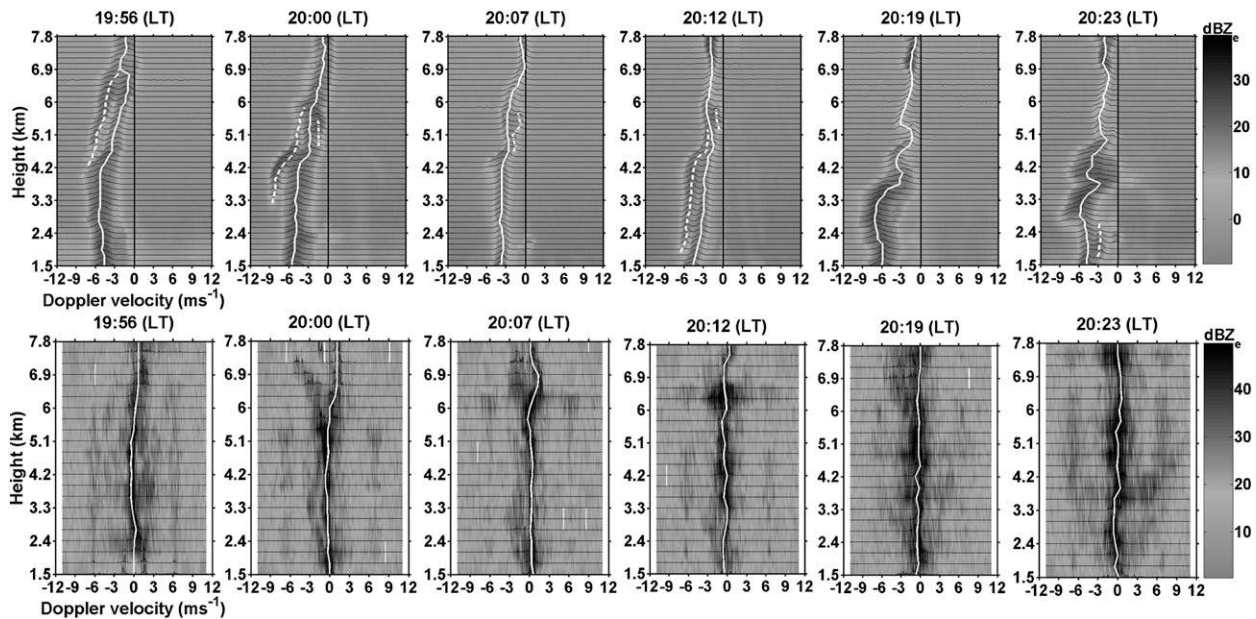
FIG. 5. The Doppler spectra of (top) LAWP and (bottom) IMSTR during the period corresponding to box 1. (top) The traces of primary, secondary, and tertiary peaks in the precipitation echo are shown with solid, dashed, and dash–dot lines. The solid line on IMSTR spectra indicates the trace of clear-air echo, which in turn provides the vertical air motion information.

clearly show the coexistence of two (three on occasions and at few range gates) distinct modes of different fall velocities. At 1956 LT, the Doppler velocity of the mode shown with the solid line on LAWP spectra increases gradually with decreasing altitude in the height region of 4.65–6.75 km with a gradient of 1.5 m s^{-1} km^{-1}. The Doppler velocity is also >3 m s^{-1} at about 5.1 km. The riming can produce such strong gradients in Doppler velocity and large Doppler velocities above the melting level (Zawadzki et al. 2001). However, the vertical air velocity profile, obtained with the IMSTR, also shows strong gradient (~0.75 m s^{-1} km^{-1}) in the same height region. Although the gradient in vertical air motion explains half of the gradient in Doppler velocity of hydrometeors, the fall velocity of hydrometeors (after correcting the Doppler velocity for vertical air motion) at around 5 km is still large (>2.8 m s^{-1}), and supports the above explanation that the riming is occurring predominantly in that height region. The second mode (dashed line) also supports that the riming is the primary process for the hydrometeor growth in this case, as this mode shows large values and also varies about 4.5 m s^{-1} in a height region of 2.2 km (i.e., 2.66, 7.36 m s^{-1} at 6.75 and 4.2 km, respectively). There is no considerable change in the first mode (solid line) from 1956 to 2000 LT, however, the second mode (dashed line) seems to be shifted down in height. Another mode (i.e., the dash–dot line) is noticed in the height range of 4.8–5.4 km during 1956–2012 LT. At 1956 LT, this mode is observed

only at two range gates: 4.65 and 4.8 km (therefore not shown in the figure). Given that the riming is occurring predominantly during this period and supercooled water is a prerequisite for riming, the third mode can be thought of associated with supercooled cloud particles. The IMSTR also shows updraft above 5.4 km, another condition ideal for the formation of supercooled water.

It is imperative to find possible sources of multi-modality in rain DSD to better understand this issue. As riming seems to be the predominant process in this case, the enhancement in reflectivity and Doppler velocity is not as prominent as one expects in the stratiform rain (Rao et al. 2008). In other words, because of riming the size, density, and Doppler velocity of hydrometeors became larger above the melting level itself and, therefore, no significant change in reflectivity and Doppler velocity is observed in the melting layer. Nevertheless, it is clear that the two observed modes are associated with solid hydrometeors (primarily snowflakes). These solid hydrometeors generally consume most of the cloud liquid water for its growth and inhibit the cloud liquid particles to grow bigger. However, when the ice crystal concentration reduces, they may be insufficient to consume the entire cloud liquid water. In such conditions, the cloud liquid particles grow to a size, detectable by the radar, as shown in subsequent spectra in Fig. 5.

At 2012 LT 21 June 2000 (Fig. 5), two traces (solid and dashed lines) are clearly visible below 5.1 km in the LAWP spectra. The mode represented by the solid line
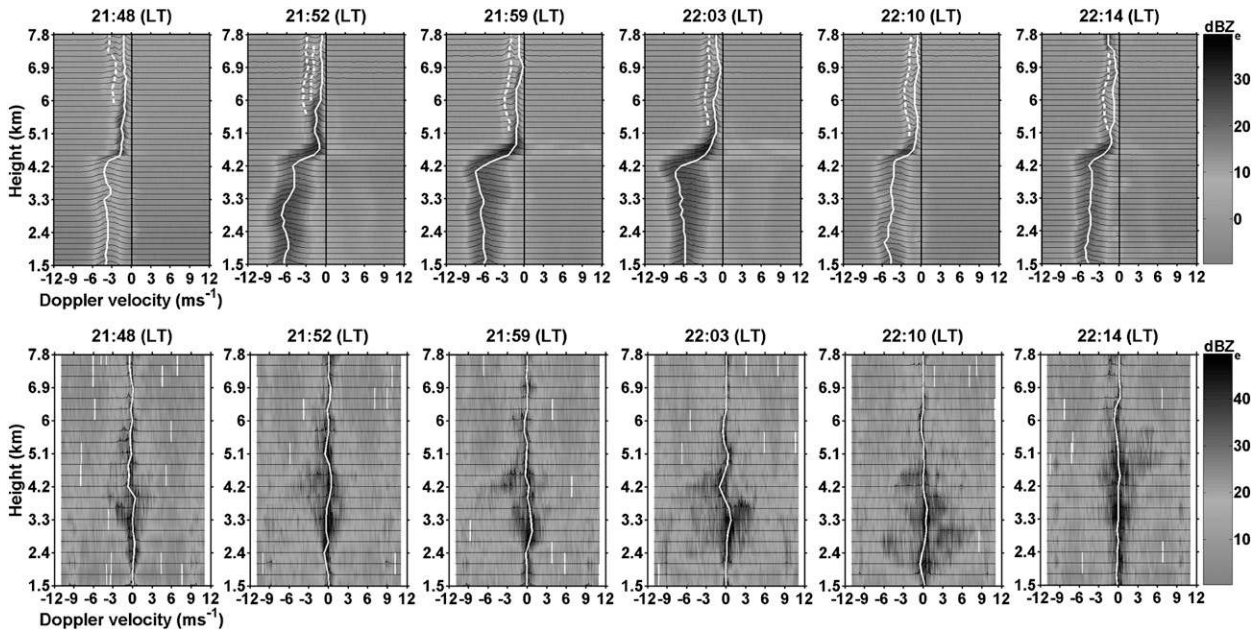
FIG. 6. As in Fig. 5, but for the period corresponding to box 2.

does not show any significant enhancement in reflectivity and Doppler velocity. This mode is associated with liquid hydrometeors, as discussed above, whereas the other mode showing enhancements in Doppler velocity and reflectivity is associated with solid hydrometeors. The subsequent spectra (at 2019 and 2023 LT) show large variations in Doppler velocity with altitude. During this period, the MRDSD is observed only at few range gates.

Figure 6 shows the IMSTR and LAWP spectra corresponding to box 2, the period in which the amplitude of undulations in vertical velocity is smaller than the amplitude during the period corresponding to box 1. The precipitation is mostly of stratiform in nature with the bright band persisting through out this period, albeit with varying intensity and thickness. Figure 6 clearly depicts the bimodal rain DSD above the radar bright band. It is interesting to note that the bimodality persisted for ∼30 min and also the traces (solid and dashed lines) of both modes are almost continuous with altitude. The high mode observations of LAWP indicate (not shown) that the bimodality, in fact, has started at a much higher altitude than shown in the Fig. 6. Except for a short duration centered at 2203 LT, the bimodal rain DSD is hardly seen below the bright band during this period. The source for this bimodal distribution is unclear. The secondary ice generation by the Hallet–Mossop mechanism (Mossop 1976) can be ruled out because the temperatures at which the bimodality started are too low for this process to occur. The supercooled

water and ice crystals can coexist under certain conditions (Zawadzki et al. 2000) and can produce such bimodality. If they coexist, one would expect bimodal distribution below the bright band, as observed at 2012 LT 21 June 2000 (Fig. 5). Also, the reflectivity and Doppler velocity profiles show sharp enhancements at the bright band indicating that these modes are associated with solid hydrometeors. Interestingly, the reflectivity corresponding to the mode with a smaller fall velocity is higher than that of the other mode. Given the large dependence of reflectivity on drop diameter ($Z_e \propto D^6$), big (small) hydrometeors, generally having larger (smaller) fall velocities, produce strong (weak) backscatter. The exceptions, however, are the low-density large ice flakes (large ice flakes with air gaps) and nonspherical hydrometeors at stratiform rainfall rates (Fabry and Zawadzki 1995). Hydrometeors of this type produce large radar backscatter because of their large radar cross section but fall with smaller velocities. Therefore, the mode represented by the solid line may be associated with such hydrometeors. The other possibility is that the hydrometeors associated with the second mode (dashed line) are bigger in size (enough to be observed by the radar) but fewer in number.

The MRDSD can also occur in the radar spectra taken during the transition period (Figs. 1, 7, and 8). The transition can be from one streamer to the other within the stratiform rain (Fig. 7), as evidenced from the bright-band structure (Fig. 3) and weak rainfall. The transition can also be from light rain to intense convection (Fig. 8).
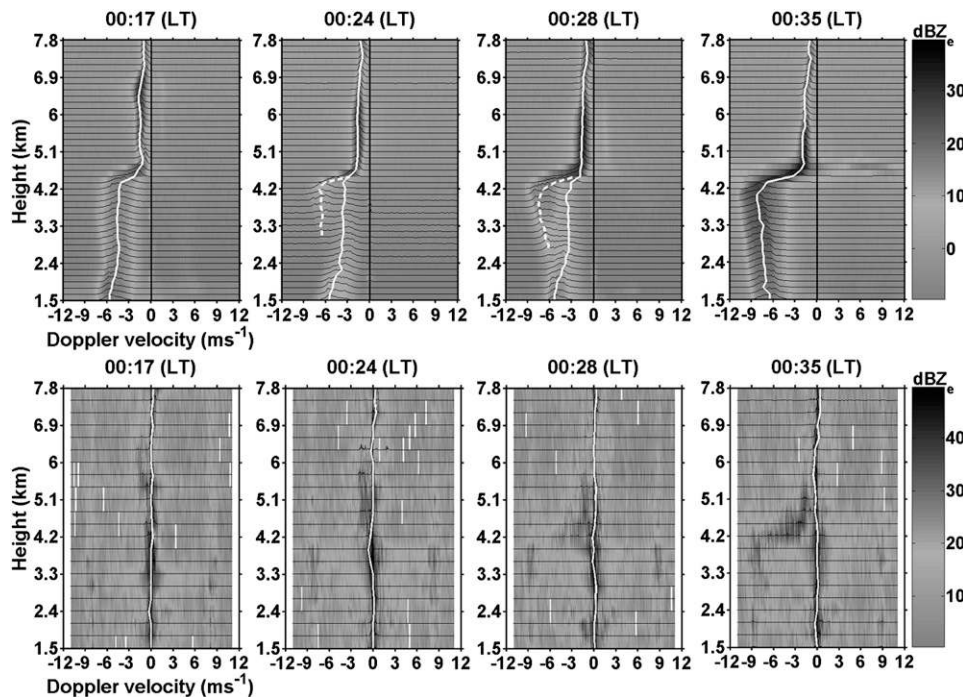
FIG. 7. As in Fig. 5, but for the period corresponding to box 3.

Most of the time, they occur only at few range gates and for short duration. Note that the vertical velocity field is completely different during these periods. The rain during the period corresponding to box 3 represents the stratiform rain (Fig. 7) and therefore has weak up/downdrafts. On the other hand, the period corresponding to box 4 is associated with intensifying convection and therefore large vertical velocities (8–10 m s^{-1}) are prevalent during this period.

Interestingly the Doppler spectra during the period corresponding to box 5 (Fig. 9), the period when high-amplitude gravity waves are prevalent, have striking similarity with the Doppler spectra in Fig. 5. In the initial phase of the observation period (2248–2300 LT), two distinct modes of velocities are clearly observed above the freezing level. They are associated with solid hydrometeors as evidenced from their increase in reflectivity and Doppler velocity in the vicinity of the melting level. Similar to Fig. 5, a bimodal distribution below the bright band is observed after the second mode disappeared. The two modes seen below the freezing level after 2311 LT are the result of the backscatter from melting/melted ice flakes and supercooled droplets.

To further investigate the altitude variation of MRDSD, height profiles of rain DSD are considered (Fig. 10). The top (bottom) panel corresponds to the height variation of rain DSD at various stages of decaying convection/transition region, during the period

1956–2023 LT (2256–2322 LT) 21 (22) June 2000. As can be seen from the figure that DSD is retrieved only for the rain regime (i.e., below 3.6 km). The distribution of rain DSD is highly variable with time on 21 June 2000, just like the rain on that day. The rain is also weak on that day, which further created problems in retrieving rain DSD for few spectra. Nevertheless, a bimodal distribution is clearly seen at 2012 LT at all heights: one mode is at the lower drop end (0.5–0.6 mm) and the other is at ~1.2 mm. The distribution shows little variation with altitude. The rain DSD distribution at the surface (during 2019–2024 LT; Fig. 2a) also show peaks at the same diameters, indicating that the MRDSD observed aloft reached the ground without many changes. Nissen et al. (2005) also observed little variation of rain DSD with altitude in weak–moderate rain and attributed it to the weak interaction between raindrops. The rainfall rate is relatively higher on 22 June 2000 and therefore the distribution of rain DSD is also broader. Raindrops bigger than 2.5 mm are observed at aloft and also on the surface. Figure 10 clearly depicts the multimodal distribution during most of the observational period on 22 June 2000, but it is much clearer and prominent at 2318 and 2322 LT. The peaks in the distribution, however, appear at different diameters relative to the peaks observed on 21 June 2000. On 22 June 2000, the peak at the smaller drop end is not very clear as it is very close to the lower limit of the DSD derived with the radar. The
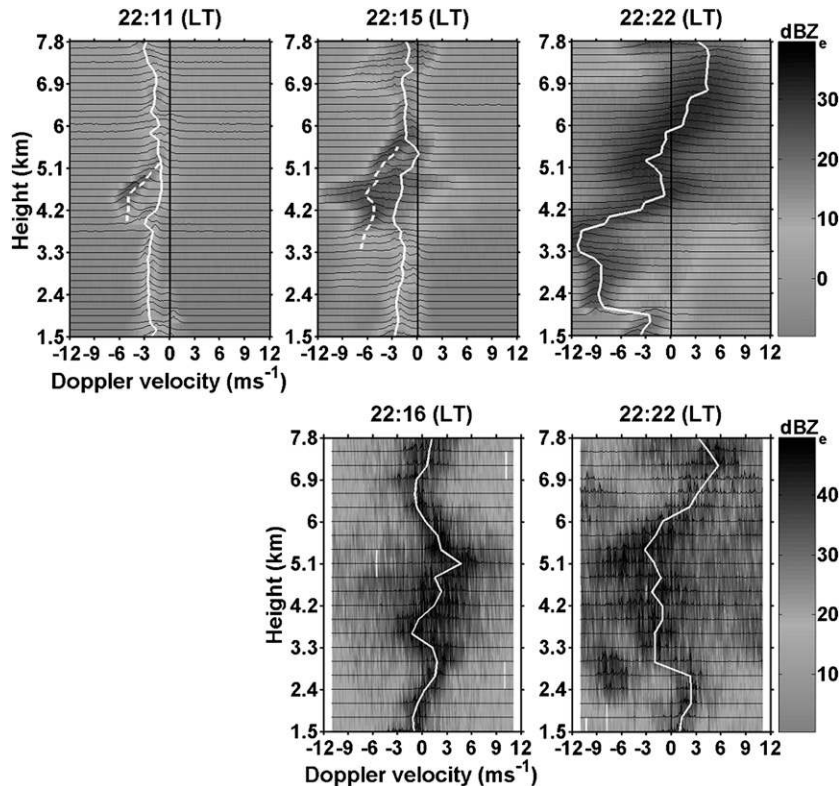
FIG. 8. As in Fig. 5, but for the period corresponding to box 4.

other peak, which is at ~1.8–2.2 mm, is consistent with earlier theoretical and experimental results (Steiner and Waldvogel 1987; McFarquhar 2004). Corresponding drop size spectra near the surface (during 2325–2329 LT) also show peak at ~1.8 mm, confirming that the peaks in the distribution are not shifting significantly with altitude.

4. Summary

The IMSTR, LAWP, and JW disdrometer measurements are utilized to investigate the source mechanisms of MRDSD aloft in the radar spectra and at the surface. Earlier reports on MRDSD using vertically pointing radars are limited to stratiform rain (Gossard et al. 1990; Zawadzki et al. 2001). For the first time an attempt has been made to address the key questions related to the occurrence of MRDSD during the passage of a MCS, which includes two convective storms. For example, in a MCS, what are the preferential stages and heights at which bi- or multimodal rain distributions are seen? The two convective storms under observation are distinctly different in terms of the total rainfall and rainfall rate generated by them. However, the vertical wind field is nearly similar during the passage of both

the storms, in general, the maximum vertical wind and the gravity wave pattern, in particular (Dhaka et al. 2003).

The MRDSD is observed continuously at times and intermittently on few occasions. On several occasions, the peaks in the distribution migrated toward the lower drop end (Fig. 2). The radar maps also show that the MRDSD propagates down with time. On a few occasions, the rain DSD has not changed much with altitude (Fig. 10). In particular, the rain DSD is nearly similar at all altitudes and also at the surface, when the bimodal distribution is arising due to the melting of ice flakes and supercooled droplets (2012 LT 21 June 2000 and 2318 and 2322 LT 22 June 2000).

The earlier studies considered several mechanisms to explain the MRDSD, starting from breakup of ice habits (Donaldson 1984; Valdez and Young 1985; List et al. 1987; Brown 1988; McFarquhar 2004) to the overlapping of rain shafts (Sauvageot and Koffi 2000) and to the coexistence of ice and SCW (Zawadzki et al. 2001). In reality, the observed MRDSD is the result of complex interplay of all these mechanisms, as these processes feedback on each other. It is possible to infer some of the above processes from the present observations. For example, the bimodality below the freezing
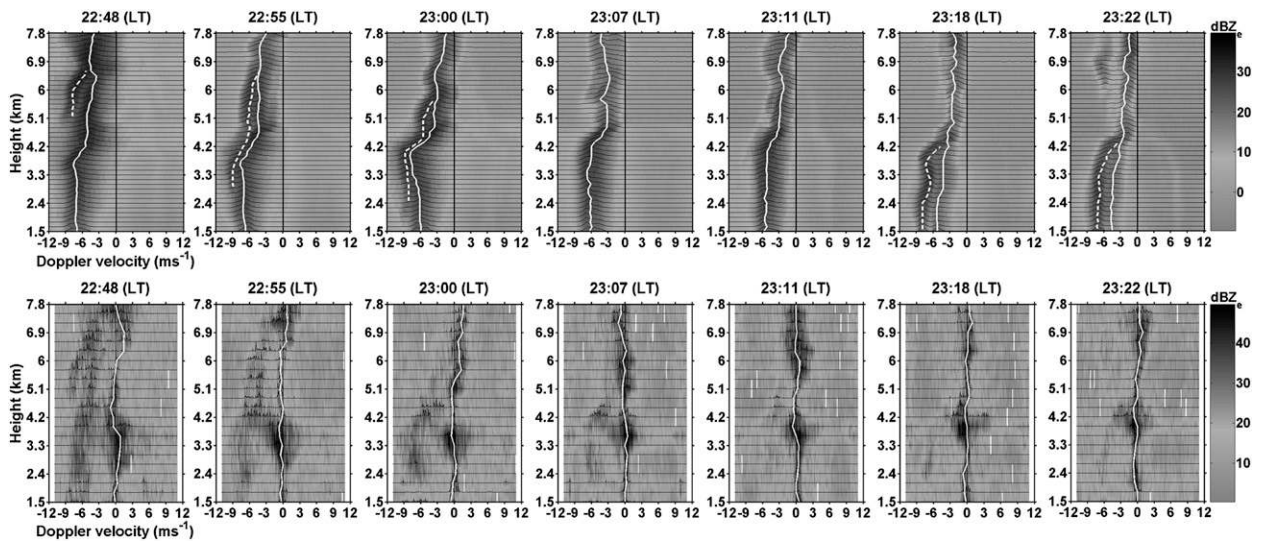
FIG. 9. As in Fig. 5, but for the period corresponding to box 5.

level is attributed to the coexistence of melted ice flakes and supercooled droplets. The bimodality in Fig. 6 is mostly observed above the freezing level and persisted for about 30 min. However, the source of this bimodality is not clear.

The MRDSD and its variation are strikingly similar in both the storms in the decaying period (i.e., transition stage from convection to stratiform rain). During this period, the MRDSD is observed initially at higher levels (e.g., 6–7 km), and then at lower levels in the subsequent spectra. A few minutes later, the bimodality appeared again at and below the freezing level due to the coexistence of snow and supercooled droplets. It is thus clear from the present observations that the transition period

from the convection to stratiform rain is the most prone zone for MRDSD to occur (Figs. 5 and 9). The other prominent zone for the occurrence of bimodality is the transition period, where the DSDs of decaying and intensifying streamers overlap (Figs. 7 and 8). In such events, the bimodality is observed only for short duration or/and at a few altitudes.

The present study has several practical implications, but most importantly, it has shown that the supercooled water and ice will coexist in the later part of the transition region. Such information will be very useful for aviation industry. The presence of supercooled water can lead to hazardous conditions for aircraft, such as aircraft icing, air craft malfunctioning, and excess fuel
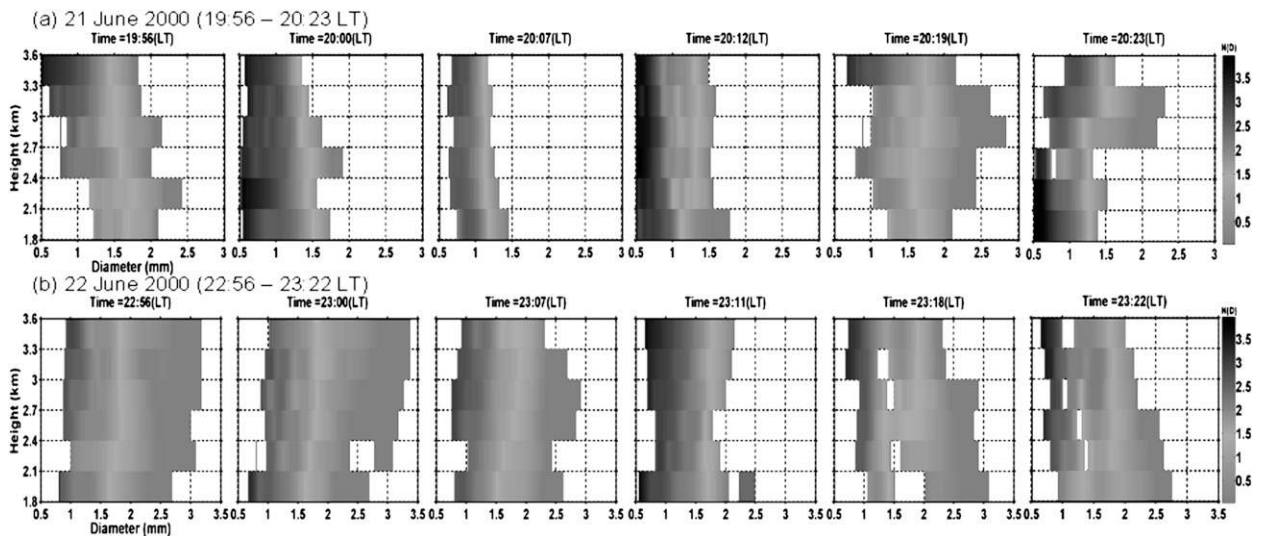

FIG. 10. (a), (b) The altitudinal variation of rain DSD corresponds to the Doppler spectra shown in Figs. 5 and 9, respectively.

consumption; therefore, accurately forecasting and understanding regions of potential icing is required for flight planning. Such attempts have been made through modeling studies (Zawadzki et al. 1993; Tremblay et al. 1995) and radar measurements (Zawadzki et al. 2001). It is also feasible to diagnose locally the presence and the amount of supercooled liquid water coexisting with snow if a good estimate of the vertical motion is available, and if the amount of snow is known with sufficient accuracy. Although vertical air motion information is available to us, the temperature and humidity profiles are not available for estimating the amount of snow, as estimated in Zawadzki et al. (2001). Such studies will be taken up in the near future. Also, the multipeak behavior of the raindrop size distribution needs to be studied statistically as a function of the rain rate to better understand the MRDSD.

REFERENCES

Atlas, D., and V. G. Plank, 1953: Drop-size history during a shower. *J. Meteor.,* **10,** 291–295.

——, R. C. Srivastava, and R. S. Sekhon, 1973: Doppler radar characteristics of precipitation at vertical incidence. *Rev. Geophys. Space Sci.,* **11,** 1–35.

Brown, P. S., Jr., 1988: The effects of filament, sheet, and disk breakup upon the drop spectrum. *J. Atmos. Sci.,* **45,** 712–718.

Dhaka, S. K., M. Takahashi, Y. Kawatani, S. Malik, Y. Shibagaki, and S. Fukao, 2003: Observations of deep convective updrafts in tropical convection and their role in the generation of gravity waves. *J. Meteor. Soc. Japan,* **81,** 1185–1199.

Donaldson, N. R., 1984: Raindrop evolution with collision breakup: Theory and models. Ph.D. thesis, University of Toronto, Toronto, Ontario, Canada, Canadian Thesis No. 66758, 181 pp. [Available from the National Library of Canada, 395 Wellington St., Ottawa, ON K1A 0N4, Canada.]

Douglas, R. H., K. L. S. Gunn, and J. S. Marshall, 1957: Pattern in the vertical of snow generation. *J. Meteor.,* **14,** 95–114.

Fabry, F., and I. Zawadzki, 1995: Long-term radar observations of the melting layer of precipitation and their interpretation. *J. Atmos. Sci.,* **52,** 838–851.

Feingold, G., and Z. Levin, 1986: The lognormal fit to raindrop spectra from frontal convective clouds in Israel. *J. Climate Appl. Meteor.,* **25,** 1346–1363.

Foote, G. B., and P. S. du Toit, 1969: Terminal velocity of raindrops aloft. *J. Appl. Meteor.,* **8,** 249–253.

Gage, K. S., C. R. Williams, P. E. Johnston, W. L. Ecklund, R. Cifelli, A. Tokay, and D. A. Carter, 2000: Doppler radar profiles as calibration tools for scanning radars. *J. Appl. Meteor.,* **39,** 2209–2222.

Garcia-Garcia, F., and J. E. Gonzalez, 2000: Raindrop spectra observations from convective showers in the valley of Mexico. *Proc. 13th Int. Conf. on Clouds and Precipitation,* Reno, NV, International Commission on Cloud Physics and International Association for Meteorology and Precipitation, 398–401.

Gossard, E. E., R. G. Strauch, and R. R. Rogers, 1990: Evolution of drop size distribution in liquid precipitation observed by ground-based Doppler radar. *J. Atmos. Oceanic Technol.,* **7,** 815–828.

Gunn, K. L. S., and J. S. Marshall, 1955: The effect of wind shear on falling precipitation. *J. Meteor.,* **12,** 339–349.

Joss, J., and A. Waldvogel, 1967: Ein Spektrograph für Niederschlagstropfen mit automatischer Auswertung. *Pure Appl. Geophys.,* **68,** 240–246.

——, and ——, 1969: Raindrop size distribution and sampling size errors. *J. Atmos. Sci.,* **26,** 566–569.

Kirankumar, N. V. P., T. N. Rao, B. Radhakrishna, and D. N. Rao, 2008: Statistical characteristics of raindrop size distribution in southwest monsoon season. *J. Appl. Meteor. Climatol.,* **47,** 576–590.

Kollias, P., B. A. Albrecht, and F. D. Marks Jr., 2001: Raindrop sorting induced by vertical drafts in convective clouds. *Geophys. Res. Lett.,* **28,** 2787–2790.

List, R., N. R. Donaldson, and R. E. Stewart, 1987: Temporal evolution of drop spectra to collisional equilibrium in steady and pulsating rain. *J. Atmos. Sci.,* **44,** 362–372.

Low, T. B., and R. List, 1982a: Collision, coalescence, and breakup of raindrops. Part I: Experimentally established coalescence efficiencies and fragment size distributions in breakup. *J. Atmos. Sci.,* **39,** 1591–1606.

——, and ——, 1982b: Collision, coalescence, and breakup of raindrops. Part II: Parameterization of fragment size distributions. *J. Atmos. Sci.,* **39,** 1607–1618.

Lucas, C., A. D. MacKinnon, R. A. Vincent, and P. T. May, 2004: Raindrop size distribution retrievals from a VHF boundary layer profiler. *J. Atmos. Oceanic Technol.,* **21,** 45–60.

Marshall, J. S., 1953: Precipitation trajectories and patterns. *J. Meteor.,* **10,** 25–29.

——, and W. M. Palmer, 1948: The distribution of raindrops with size. *J. Meteor.,* **5,** 165–166.

McFarquhar, G. M., 2004: A new representation of collision-induced breakup of raindrops and its implications for the shapes of raindrop size distributions. *J. Atmos. Sci.,* **61,** 777–794.

——, and R. List, 1991: The evolution of three-peak raindrop size distributions in one-dimensional shaft model. Part II: Multiple pulse rain. *J. Atmos. Sci.,* **48,** 1587–1595.

——, and ——, 1993: The effect of curve fits for the disdrometer calibration on raindrop spectra, rainfall rate, and radar reflectivity. *J. Appl. Meteor.,* **32,** 774–782.

——, ——, D. R. Hudak, R. P. Nissen, and J. S. Dobbie, 1996: Flux measurements of pulsating rain with a disdrometer and Doppler radar during phase II of the joint tropical rain experiment in Malaysia. *J. Appl. Meteor.,* **35,** 859–874.

Mossop, S. C., 1976: Production of secondary ice particles during the growth of graupel by riming. *Quart. J. Roy. Meteor. Soc.,* **102,** 45–57.

Nissen, R., R. List, D. Hudak, G. M. McFarquhar, R. P. Lawson, N. P. Tung, S. K. Soo, and T. S. Kang, 2005: Constant raindrop fall speed profiles derived from Doppler radar data analyses for steady nonconvective precipitation. *J. Atmos. Sci.,* **62,** 220–230.

Prat, O. P., and A. P. Barros, 2007: A robust numerical solution of the stochastic collection–breakup equation for warm rain. *J. Appl. Meteor. Climatol.,* **46,** 1480–1497.

Rajopadhyaya, D. K., P. T. May, and R. A. Vincent, 1993: A general approach to the retrieval of raindrop size distributions from VHF wind profiler Doppler spectra: Modeling results. *J. Atmos. Oceanic Technol.,* **10,** 710–717.

Ralph, F. M., 1995: Using radar-measured radial vertical velocities to distinguish precipitation scattering from clear-air scattering. *J. Atmos. Oceanic Technol.,* **12,** 257–267.

Rao, P. B., A. R. Jain, P. Kishore, P. Balamuralidhar, S. H. Damle, and G. Viswanathan, 1995: Indian MST radar, 1. System description and sample vector wind measurements in ST mode. *Radio Sci.,* **30,** 1125–1138.

Rao, T. N., D. N. Rao, and S. Raghavan, 1999: Tropical precipitating systems observed with Indian MST radar. *Radio Sci.,* **5,** 1125–1139.

——, ——, K. Mohan, and S. Raghavan, 2001: Classification of tropical precipitating systems and associated *Z-R* relationships. *J. Geophys. Res.,* **106,** 17 699–17 711.

——, N. V. P. Kirankumar, B. Radhakrishna, and D. N. Rao, 2006: On the variability of the shape-slope parameter relations of the gamma raindrop size distribution model. *Geophys. Res. Lett.,* **33,** L22809, doi:10.1029/2006GL028440.

——, ——, ——, ——, and K. Nakamura, 2008: Classification of tropical precipitating systems using wind profiler spectral moments: I. Algorithm description and validation. *J. Atmos. Oceanic Technol.,* **25,** 884–897.

Sauvageot, H., and M. Koffi, 2000: Multimodal raindrop size distributions. *J. Atmos. Sci.,* **57,** 2480–2492.

Schafer, R., S. Avery, P. May, D. Rajopadhyaya, and C. Williams, 2002: Estimation of rainfall drop size distributions from dual frequency wind profiler spectra using deconvolution and a nonlinear least squares fitting technique. *J. Atmos. Oceanic Technol.,* **19,** 864–874.

Sheppard, B. E., 1990: Effect of irregularities in the diameter classification of raindrops by the Joss–Waldvogel disdrometer. *J. Atmos. Oceanic Technol.,* **7,** 180–183.

Steiner, M., and A. Waldvogel, 1987: Peaks in raindrop size distributions. *J. Atmos. Sci.,* **44,** 3127–3133.

Testik, F. Y., and A. P. Barros, 2007: Toward elucidating the microstructure of rainfall: A survey. *Rev. Geophys.,* **45,** RG2003, doi:10.1029/2005RG000182.

Tokay, A., and D. A. Short, 1996: Evidence from tropical raindrop spectra of the origin of rain from stratiform versus convective clouds. *J. Appl. Meteor.,* **35,** 355–371.

Tremblay, A., A. Glazer, W. Szyrmer, G. Isaac, and I. Zawadzki, 1995: Forecasting of supercooled clouds. *Mon. Wea. Rev.,* **123,** 2098–2113.

Ulbrich, C. W., 1983: Natural variations in the analytical form of the raindrop size distribution. *J. Climate Appl. Meteor.,* **22,** 1764–1775.

Valdez, M. P., and K. C. Young, 1985: Number fluxes in equilibrium raindrop populations: A Markov chain analysis. *J. Atmos. Sci.,* **42,** 1024–1036.

Wakasugi, K., A. Mizutani, M. Matsuo, S. Fukao, and S. Kato, 1986: A direct method for deriving drop-size distribution and vertical air velocities from VHF Doppler radar spectra. *J. Atmos. Oceanic Technol.,* **3,** 623–629.

Williams, C. R., W. L. Ecklund, and K. S. Gage, 1995: Classification of precipitating clouds in the tropics using 915-MHz wind profilers. *J. Atmos. Oceanic Technol.,* **12,** 996–1012.

Willis, P. T., 1984: Functional fits to some observed drop size distributions and parameterization of rain. *J. Atmos. Sci.,* **41,** 1648–1661.

Zawadzki, I., and M. De A. Antonio, 1988: Equilibrium raindrop size distributions in tropical rain. *J. Atmos. Sci.,* **45,** 3452–3459.

——, L. Ostiguy, and J. P. R. Laprise, 1993: Retrieval of the microphysical properties in CASP storm by integration of a numerical kinematic model. *Atmos.–Ocean,* **31,** 201–233.

——, W. Szyrmer, and S. Laroche, 2000: Diagnostic of supercooled cloud from single Doppler observations in regions of detectable snow. *J. Appl. Meteor.,* **39,** 1041–1058.

——, F. Fabry, and W. Szyrmer, 2001: Observations of supercooled water and secondary ice generation by a vertically pointing X-band Doppler radar. *Atmos. Res.,* **59–60,** 343–359.